A comprehensive study of the glass/translucent anti-glass/transparent ceramic structural ordering in the Bi2O3Nb2O5–TeO2 system

Morgane Dolhen, Mathieu Allix, Vincent Sarou-Kanian, Franck Fayon, Cécile Genevois, Sébastien Chenu, Pierre-Eugène Coulon, Maggy Dutreilh-Colas, Julie Cornette, Jean-René Duclere, et al.

A comprehensive study of the glass / translucent anti-glass / transparent ceramic structural ordering in the Bi_2O_3-Nb_2O_5-TeO_2 system

Morgane Dolhen[1], Mathieu Allix[2], Vincent Sarou-Kanian[2], Franck Fayon[2], Cécile Genevois[2], Sébastien Chenu[1], Pierre-Eugène Coulon[3], Maggy Colas[1], Julie Cornette[1], Jean-René Duclère[1], François Brisset[4], Olivier Masson[1], Philippe Thomas[1], Gaëlle Delaizir[1]

[1] *Institut de Recherche sur les Céramiques (IRCER), UMR 7315, Université de Limoges, Centre Européen de la Céramique, Limoges, France*

[2] *Conditions Extrêmes et Matériaux : Haute Température et Irradiation (CEMHTI), UPR3079 CNRS, Orléans, France*

[3] *Laboratoire des Solides Irradiés, Ecole Polytechnique, Palaiseau, France*

[4] *Institut de Chimie Moléculaire et des Matériaux d'Orsay (ICMMO), UMR 8182 CNRS, Orsay, France*

Abstract

The full and congruent crystallization of the $Bi_{0.8}Nb_{0.8}Te_{2.4}O_8$ (BNT) glass leads to perfectly transparent ceramic in both the visible and near infrared ranges. While heating the parent glass, an intermediate structural regime order – called anti-glass – that shows chemical inhomogeneity at the nanometer scale and with a long-range cationic ordering while retaining a strong local anionic disorder is observed. Here, we report on the crystallization sequence starting from the $Bi_{0.8}Nb_{0.8}Te_{2.4}O_8$ glass system and show that an intermediate $Bi_{0.8}Nb_{0.8}Te_{2.4}O_8$ anti-glass phase (polymorph 1) is first formed, before transforming into a more ordered and ceramic material (polymorph 2). In particular, we provide a comprehensive structural study of the crossover between glass and its crystalline counterpart through intermediate steps. Similarities and differences between the structures, microstructures of $Bi_{0.8}Nb_{0.8}Te_{2.4}O_8$ glass, anti-glass and ceramic materials of identical composition are investigated in details at different length scales

by X-ray and neutron powder diffraction, SEM-EBSD, TEM, NMR and Raman spectroscopy. The optical properties of the anti-glass and ceramic are discussed in correlation with the structure and microstructure observations. This study paves the way for understanding the complex mechanisms at the origin of the full and congruent crystallization from the parent glass.

1. Introduction

Tellurite materials are attractive for optical applications in the mid-infrared range up to 5.5 µm, including the 3-5µm atmospheric window that covers many molecular absorption bands and lying in the working region of infrared detectors. Applications of such materials, that additionally can exhibit high non-linear properties, include chemical sensors in the medical and environmental domains, optical lenses, optical fibers, optoelectronic devices, etc. [1-5]

Glasses formed in the system xBi_2O_3-xNb_2O_5-$(100-2x)TeO_2$ (x=5-12.5% mol) show formation of peculiar textures within the glassy matrix upon annealing. For example, the $7.5Bi_2O_3$-$7.5Nb_2O_5$-$85TeO_2$ glass composition, when heat-treated above its glass transition temperature, shows some micrometer scale spherulitic inclusions that exhibit the same chemical composition as the residual glassy matrix [6-8]. Such spherulites having the same composition as the matrix were observed in the Y_2O_3-Al_2O_3 system and were found to be amorphous, thus revealing polymorphism [9-12]. In contrast, the inclusions observed in these tellurite glasses exhibit narrow diffraction peaks and have been identified as an "anti-glass" phase, *i.e.*, a material showing long-range cation order but with a highly disordered anion sublattice [8, 13-16].

A second composition in this ternary system is also of great interest. The controlled crystallization of the $12.5Bi_2O_3$-$12.5Nb_2O_5$-$75TeO_2$ glass composition ($\equiv Bi_{0.8}Nb_{0.8}Te_{2.4}O_8$ also called BNT) leads to i) a translucent anti-glass material (polymorph 1) further to heat-treatment at 460°C and ii) a perfectly transparent ceramic (polymorph 2) resulting from a full and

congruent crystallization process of the parent bulk glass performed at 510°C [17]. This latter transparent ceramic material recently showed laser emission when doped with Nd^{3+} ions [18]. However, the structures of these novel $Bi_{0.8}Nb_{0.8}Te_{2.4}O_8$ anti-glass and ceramic phases have not yet been reported. Note that Qiu *et al.* recently reported the elaboration of nanoceramics fiber corresponding to the disordered anti-glass phase [19].

The initial $12.5Bi_2O_3$-$12.5Nb_2O_5$-$75TeO_2$ glass phase corresponds to a highly disordered configurational landscape that evolves towards more thermodynamically stable states during annealing. In Bi_2O_3-Nb_2O_5-TeO_2 glasses, the heavy cations with high polarizability can readily adopt positional ordered arrangement while maintaining a disordered anionic sublattice, giving rise to the metastable anti-glass phase. Then, subsequently to further heating, the anionic network is more willing to re-arrange, leading to the stable ceramic phase.

In this work, we address a thorough structural and microstructural study to understand the topological and chemical ordering taking place when heating the parent glass and leading to the elaboration of ceramics with high transparency. For this purpose, we undertook an examination of the glass / anti-glass / ceramic materials using complementary techniques allowing to probe the local or long-range averaged structures at different length scales (^{125}Te and ^{93}Nb solid-state NMR, X-ray and Neutron Powder Diffraction, Raman spectroscopy, Scanning and Transmission Electron Microscopies). It is shown that this combined approach allows an improved structural description of materials exhibiting variable and partial ordering such as anti-glass and ceramic phases.

2. Experimental

2.1 Synthesis

The $12.5Bi_2O_3$-$12.5Nb_2O_5$-$75TeO_2$ (BNT) glass composition was synthesized in a platinum crucible from high purity precursors (TeO_2 Alfa Aesar 99.99%, Bi_2O_3 Sigma Aldrich 99,99%,

Nb_2O_5 Sigma Aldrich 99.99%) using the melt-quenching technique. A ~ 2g mixture was heat-treated at 850°C for 15 minutes with intermediate stirring and then air-quenched, shaped and annealed at T_g -10°C for 2h to relax the mechanical constraints.

The anti-glass and ceramic materials were synthesized by heat-treating the bulk parent glass at 460°C for 15 minutes and 510°C for 5 minutes or 1h30 respectively.

2.2 Structural and chemical characterizations

The density of the bulk samples (glass, anti-glass and ceramic phases) was determined through the Archimedean principle using a Kern balance. This balance enables weighing solids in air (m_{air}) as well as in a solvent (in our case, water m_{water}). When the density of the buoyancy medium is known (δ_0), the density of the solid (δ) is calculated as follows:

$$\delta = \frac{m_{air}}{m_{air} - m_{water}} \delta_0 \qquad (1)$$

Differential Scanning Calorimetry (DSC) experiments were performed using TA instrument AQ20 equipment (with a heating rate of 10°C/min) to investigate the thermal properties on bulk and powdered samples.

Optical transmission measurements were carried out in the 300-3300 nm range, under normal incidence, using a Varian Cary 5000 spectrophotometer operated in a dual beam configuration. Complete refractive index dispersion curves were measured by spectroscopic ellipsometry (Horiba Jobin–Yvon UVISEL), operated at a fixed 65° incidence angle (close to the Brewster's angle). Only the refractive index value at an infinite wavelength is however reported.

Electron backscatter diffraction (EBSD) maps were recorded on the anti-glass and ceramic materials using an OIM TSL/EDAX system mounted on a FEG-SEM (Zeiss SUPRA 55 VP) system in order to confirm the absence of amorphous parts in the tellurite anti-glass and ceramic materials. The samples were optically mirror-polished prior to observations.

Laboratory X-Ray Powder Diffraction (XRD) measurements were performed using a Bragg-Brentano D8 Advance Bruker laboratory diffractometer (Cu Kα radiation) equipped with a lynxEye XE detector. Data were collected from 10 to 120° (2θ) at room temperature with a 0.012° step size and an acquisition time of 5 s per step. Room-temperature neutron powder diffraction (NPD) patterns were collected on the D2B high-resolution/high-flux powder diffractometer at the Institut Laüe-Langevin in Grenoble, France. The samples were packed in a vanadium can. Data were acquired with $\lambda = 1.59432$ Å at 2θ intervals of 0.05° over the $1° < 2\theta < 160°$ angular range. Rietveld analyses were carried out using the Jana2006 [20] software for the anti-glass phase and the Fullprof academic software which enables the use of the anisotropic broadening function [21] for the ceramic phase.

High resolution Transmission Electron Microscopy (HR-TEM) and Selected Area Electron Diffraction (SAED) were performed on a JEOL 2010F operating at 200 kV. Scanning TEM-Energy Dispersive X-ray Spectroscopy (STEM-EDS) and STEM-High Angle Annular Dark Field (STEM-HAADF) were performed using a probe-corrected (1 Å resolution) FEI Titan Themis operating at 200 kV and equipped with "Super-X" detectors. The samples were prepared prior to (S)TEM observations by Focused Ion Beam (FIB, FEI Scios).

Raman spectroscopy characterizations of the BNT glass, anti-glass and ceramic samples were performed using an In Via Reflex Renishaw Raman spectrophotometer. The spectra were recorded using a x50 objective with 785 nm wavelength excitation and low power (0.03 mW) to avoid any damage of the sample.

^{93}Nb Solid-state nuclear magnetic resonance (NMR) experiments were performed on a Bruker Avance III spectrometer operating at 20.0 T (Larmor frequency of 207.89 MHz) with a 1.3 mm magic angle sample spinning (MAS) probehead. Powdered samples were packed into rotor and spun at a MAS frequency of 65 kHz. ^{93}Nb central-transition (CT) MAS spectra were recorded using a Hahn echo sequence with a weak radio-frequency (RF) field. The echo delay was set to

615 µs allowing whole echo signal acquisition. 8192 transients were accumulated with a recycling delay of 0.5 s. Two-dimensional ^{93}Nb multiple-quantum MAS (MQMAS) spectra were recorded using the shifted-echo three-pulses sequence [22]. Triple quantum excitation and reconversion was achieved with hard pulses of 1 µs and 0.6 µs using a RF field of 160 kHz. The echo delay was set to 615 us and a RF field of 40 kHz was used for the CT-selective refocusing pulse. Depending on the sample, 20 to 40 t_1 increments synchronized with the rotor period were recorded with at least 6000 transients each using a recycling delay of 0.2 s.

^{125}Te solid-state NMR experiments were performed on Bruker Avance I spectrometer operating at 7.0 T (Larmor frequency of 94.83 MHz) using a 4 mm MAS probe. ^{125}Te static and MAS (ν_{MAS} = 14285 Hz) spectra were obtained using a Hahn echo sequence (RF field of 100 kHz) with echo delays of 200 µs and 140 µs, respectively. The recycling delay was set to 76 s for the glass and the anti-glass samples, and to 95 s for the ceramic one. At least 300 scans were accumulated for each samples. Two-dimensional Shifted Echo Phase Adjusted Spinning Sidebands [23] (PASS-SE) spectra were obtained at ν_{MAS} = 14285 Hz. 16 pitches were recorded with 250 up to 400 scans each depending on the sample. ^{93}Nb and ^{125}Te spectra were referenced using $NbCl_5$ dissolved in acetonitrile (δ= 0 ppm), and diphenyl ditelluride dissolved in $CDCl_3$ (δ= -422 ppm relatively to $Te(CH_3)_2$), respectively. Fits of ^{93}Nb and ^{125}Te 1D and 2D NMR spectra were performed with the DMfit software [24].

3. Results and discussion

3.1 Structure of BNT glass, translucent anti-glass and transparent ceramic

The $12.5Bi_2O_3$-$12.5Nb_2O_5$-$75TeO_2$ glass composition (≡ $Bi_{0.8}Nb_{0.8}Te_{2.4}O_8$) has been synthesized by the conventional melt-quenching technique at 850°C. The quenching performed in air leads to an amorphous material (parent glass) as shown by XRD (Figure 1a). The related DSC thermogram shows a glass transition temperature at around 388°C ± 2°C and two

exothermic peaks at 455°C ± 2°C and 508°C ± 2°C (onset temperature) respectively (Figure 1b). The thermograms of bulk and powdered samples are similar (SI-1) which is in favour of a preferential bulk nucleation. Our previous study showed that these two exothermic peaks correspond to the glass → anti-glass and to the anti-glass → ceramic transformations, respectively [17]. After heating the parent bulk glass at 460°C or 510°C, the materials retain an outstanding transparency as observed in Figure 1c except for the anti-glass that shows some light scattering when the sample is lifted up from the text (see photographs in Figure 1c). The optical properties of the translucent anti-glass and transparent ceramic phases will be discussed in section 3.3.

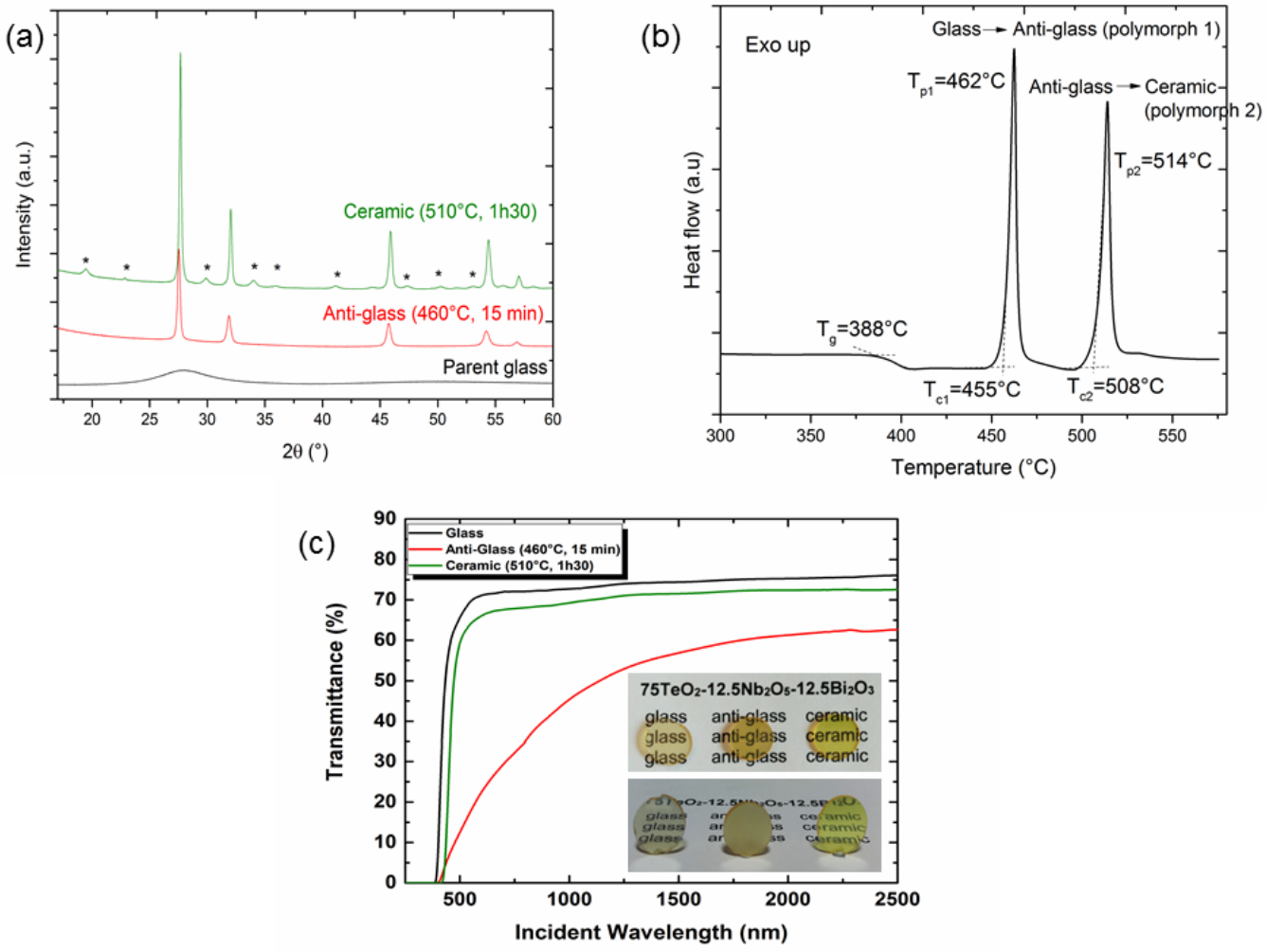

Figure 1. *(a) Powder X-Ray Diffraction (PXRD) of the parent glass (bottom), heat-treated at 460°C for 15 minutes (middle) and at 510°C for 1h30 (top). (b) DSC thermogram of the BNT parent glass, photographs of the BNT glass and glass heat-treated at 460°C for 15 minutes and 510°C for 1h30 (diameter 8 mm, thickness: 1.55mm) (c) Optical transmittance spectra of the BNT parent glass, anti-glass and ceramic materials (thickness of samples: 1.55 mm) and photographs of the samples: bulks on the text and bulks ⊥ text*

A heat-treatment performed at 460°C for 15 minutes leads to a strong crystallization of the as-prepared glass, as evidenced by XRD experiments (Figure 1a). The corresponding XRD pattern is consistent with a single crystalline phase isostructural to the cubic anti-glass β-$Bi_2Te_4O_{11}$ phase [16]. A Lebail refinement indeed matches the cubic unit cell (Fm-3m, a=5.6Å). A heat-treatment at higher temperature (510°C) for durations ranging from 5 minutes to 1h30 leads to additional XRD peaks marked with asterisks (*) as observed in Figure 1a. This indexation is still consistent with a cubic unit cell but with different space group and cell parameters (Ia-3, a=11.2Å), which appear isostructural with a MTe_3O_8 (*M*=Ti, Zr, Hf, Sn) or $A_{0.5}B_{0.5}Te_3O_8$ (with *A*=Sc, Cr, Fe, Ga, Rh, In, Bi and *B*=Nb, Ta) structural type when considering the coupled substitution $2M^{4+} \rightleftharpoons A^{3+}+B^{5+}$ [25]. Prior to EBSD experiments, the samples were polished to get rid of any potential parasite surface crystallization. EBSD performed on both anti-glass and ceramic phases confirm that the samples are fully crystallized (Figure 2). The presence of small black areas is most probably due to tearing of matter during the polishing step or to residual amorphous phase at grain boundaries at the microscopic scale. The size of the grains evolves from ~700 nm for a heat-treatment at 460°C for 15 min to 2 µm and 8 µm for the ceramics heat-treated at 510°C for 5 minutes and 1h30 respectively. In addition, it clearly appears that the microstructure of the anti-glass sample already corresponds to that of a ceramic. More precisely, in the case of the intermediate anti-glass phase, we will

refer to a translucent ceramic (polymorph 1) in opposition with the transparent ceramic (polymorph 2), which corresponds to the high temperature phase.

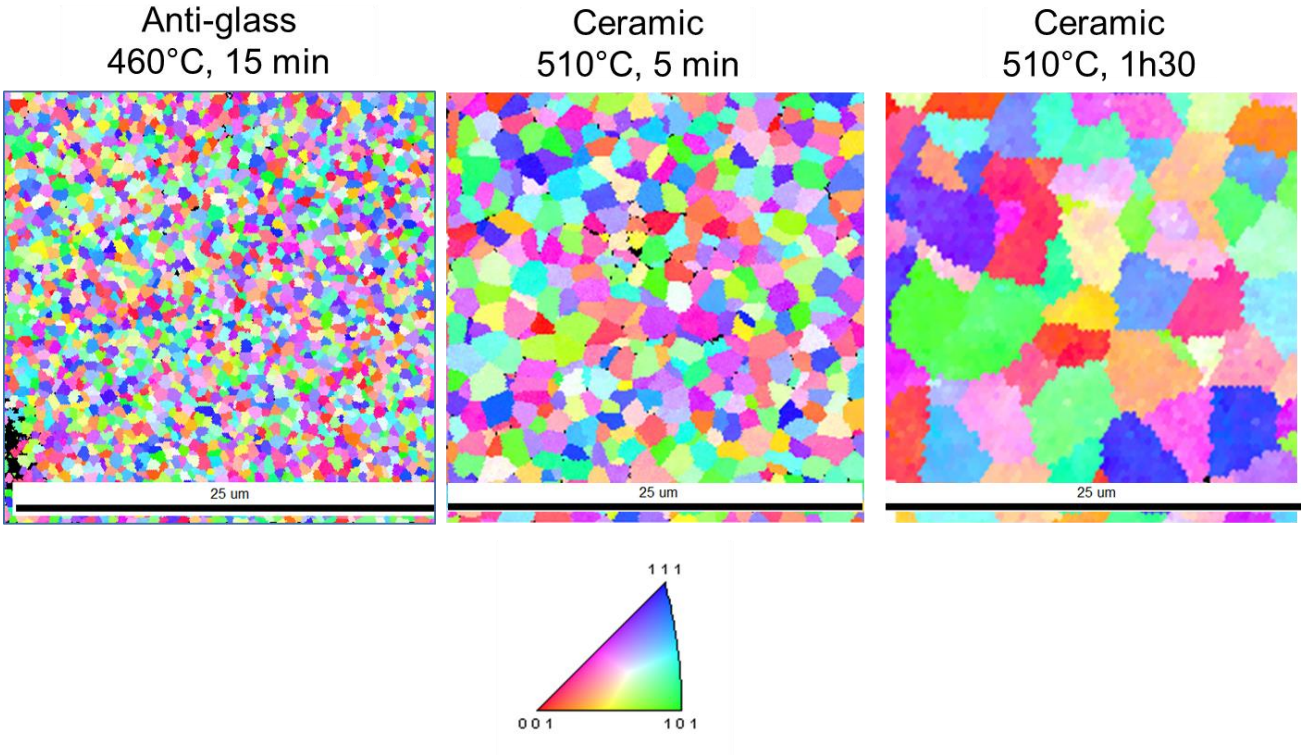

Figure 2. *EBSD of BNT parent glass heat-treated at 460°C, 15 minutes; 510°C, 5 minutes and 510°C, 1h30 (scale bar: 25 µm).*

To push further the structural characterizations, Raman spectroscopy data were collected. Raman spectra of the BNT parent glass, as well as the anti-glass and ceramics heat-treated at respectively 460°C for 15 minutes and 510°C for 5 minutes and 1h30 are shown in Figure 3. One can first observe that the Raman bands of the anti-glass sample are broad (as broad as for the initial glass) while narrow XRD peaks are visible (Figure 1a). This experimental observation reflects the existence of both high local structural disorder and long range order, thus, proving the "anti-glass" nature of this intermediate phase. The assignment of the different bands related to TeO_2-Bi_2O_3-Nb_2O_5 glasses is listed in Table 1 [8]. The gradual transformation of anti-glass into the transparent ceramic (510°C, 5 min and 1h30) upon heating leads to the narrowing of

Raman bands, in agreement with the concomitant cations and anions ordering (see further X-Ray and neutron powder diffraction data)

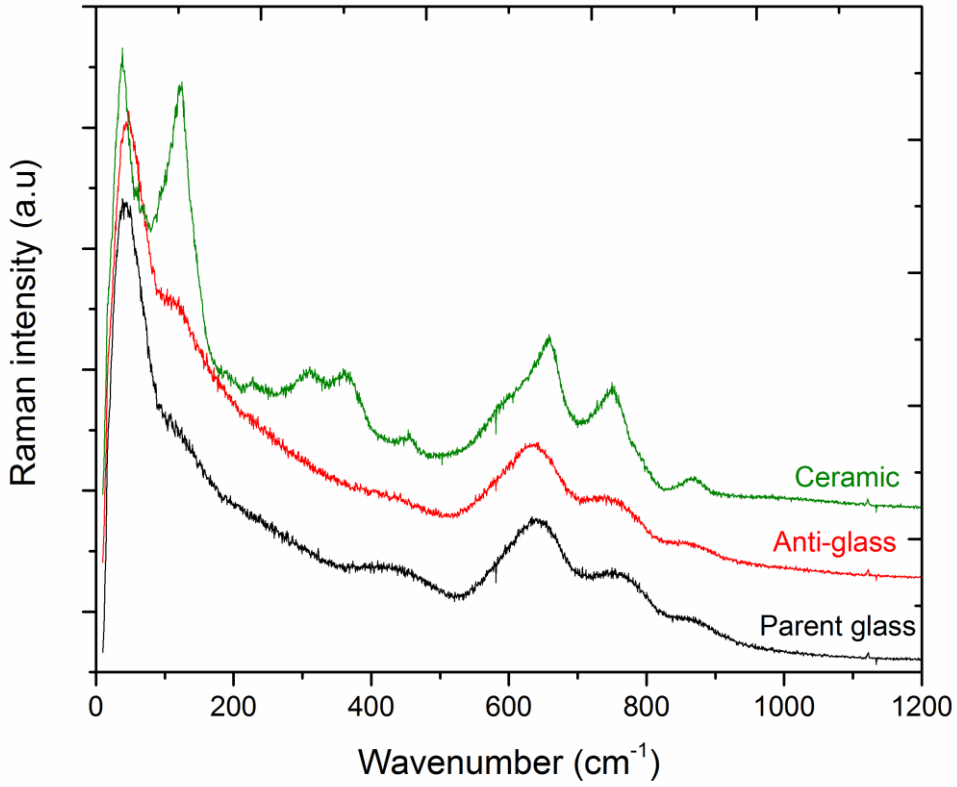

Figure 3. *Raman spectra of the parent glass (bottom) and corresponding materials heat-treated at 460°C, 15 min (anti-glass, middle) and 510°C, 1h30 (ceramic, top).*

Table 1. *Assignment of BNT Raman bands and representation of TeO_4, TeO_{3+1} and TeO_3 structural units [**8**, 26, 27]*

Wavenumber (cm^{-1})	**Raman band assignment**
110-120	Intra chain vibrations of Te-Te bonds (as in amorphous metallic t-Te)
200-400	Bending vibration of Bi-O-Bi, Nb-O-Nb, Bi-O-Te, Nb-O-Te bridges
450	Symmetric stretching of Te-O-Te and/or Bi-O-Te bridges
600	Assymmetric stretching of Te-O in TeO_4 polyhedra
650	Symmetric stretching of Te-O in both TeO_4 and TeO_3 units
720	Streching of Te-O with NBO in TeO_3 unit
770	Streching of Te-O with NBO in TeO_4 unit

880	Symmetric stretching of Nb-O in NbO_6 unit

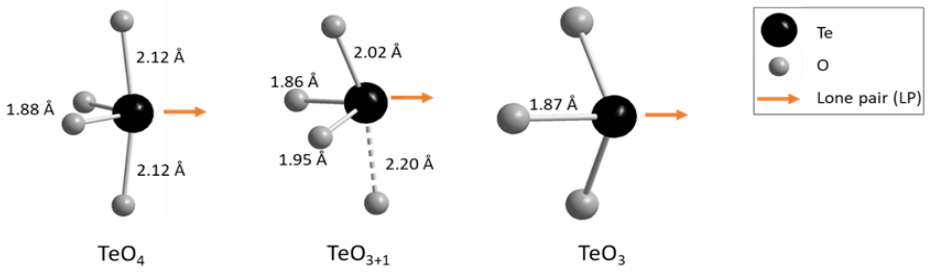

As stated earlier, the $Bi_{0.8}Nb_{0.8}Te_{2.4}O_8$ anti-glass phase appears isostructural with the cubic anti-glass β-$Bi_2Te_4O_{11}$ structure [16, 17]. As reported by Masson *et al*., although an anti-glass phase is in average isostructural with fluorite (CaF_2), its local structure cannot be precisely determined by Rietveld refinement because of the high degree of disorder in the structure, and especially a large positional disorder in the anionic network [16]. Nevertheless, a Rietveld refinement was attempted to determine an average structural model for the $Bi_{0.8}Nb_{0.8}Te_{2.4}O_8$ anti-glass phase. As expected, the X-ray diffraction data can be relatively well fitted with the cubic β-$Bi_2Te_4O_{11}$ model, using an a=5.6121(1) Å cell parameter and Fm-3m space group with a unique 4a (0, 0, 0) mixed Bi/Nb/Te cationic site. However, this model leads to a huge Debye-Weller factor for oxygen atoms, corresponding to a strong positional disorder in the anionic network as previously observed in the β-$Bi_2Te_4O_{11}$ anti-glass [16]. In order to propose a more realistic view of the $Bi_{0.8}Nb_{0.8}Te_{2.4}O_8$ anti-glass structure, the oxygen position was split into the 192*l* (x,y,z) site during refinement. The resulting Rietveld fit of the XRD data is shown in Figure 4. The refined structural parameters of the $Bi_{0.8}Nb_{0.8}Te_{2.4}O_8$ anti-glass structure are listed in Tables 2 (oxygen on 8*c* site) and 3 (oxygen split on 192*l* site) and a view of the average structure is presented in Figure 5, using both non-split and split models. The split model clearly suggests that the oxygen atoms are strongly shifted from the ideal tetrahedral sites, 8c (¼ ¼ ¼), and virtually none of them sit on 8c position. This is expected because the distance between 4a and 8c sites, ~2.43 Å ($=a\sqrt{3}/4$), is significantly larger than the typical bond lengths between Te/Bi/Nb and O atoms (~1.9-2.2Å). The disorder on the cationic sub-lattice being relatively

small, correct bond lengths necessarily require a displacement of the oxygen atoms from 8c toward the neighbouring cations. To describe more precisely the cationic local environments and their distributions in the anti-glass structure, NMR experiments have been performed and will be detailed further in this paper.

Table 2. *Atomic coordinates and occupancies determined for the $Bi_{0.8}Nb_{0.8}Te_{2.4}O_8$ anti-glass phase from Rietveld refinement of X-ray powder diffraction patterns collected at room temperature.*[a]

Atom	Site	x	y	z	Occupancy	U_{iso} (Å²)
Nb1	4a	0	0	0	0.2[b]	0.082(1)
Bi1	4a	0	0	0	0.2[b]	0.082(1)
Te1	4a	0	0	0	0.6[b]	0.082(1)
O1	8c	0.25	0.25	0.25	1	>0.1

[a] Space group Fm-3m, a=5.6121(1) Å. [b] Fixed parameter.

Table 3. *Atomic coordinates and occupancies determined for the $Bi_{0.8}Nb_{0.8}Te_{2.4}O_8$ anti-glass phase from Rietveld refinement of X-ray powder diffraction patterns collected at room temperature and considering a site splitting model for the oxygen position.*[a]

Atom	Site	x	Y	Z	Occupancy	U_{iso} (Å²)
Nb1	4a	0	0	0	0.2[b]	0.08(1)
Bi1	4a	0	0	0	0.2[b]	0.08(1)
Te1	4a	0	0	0	0.6[b]	0.08(1)
O1	192l	0.28(6)	0.33(3)	0.33(4)	0.08333	0.09(1)

[a] Space group Fm-3m, a=5.6121(2) Å. [b] Fixed parameter.

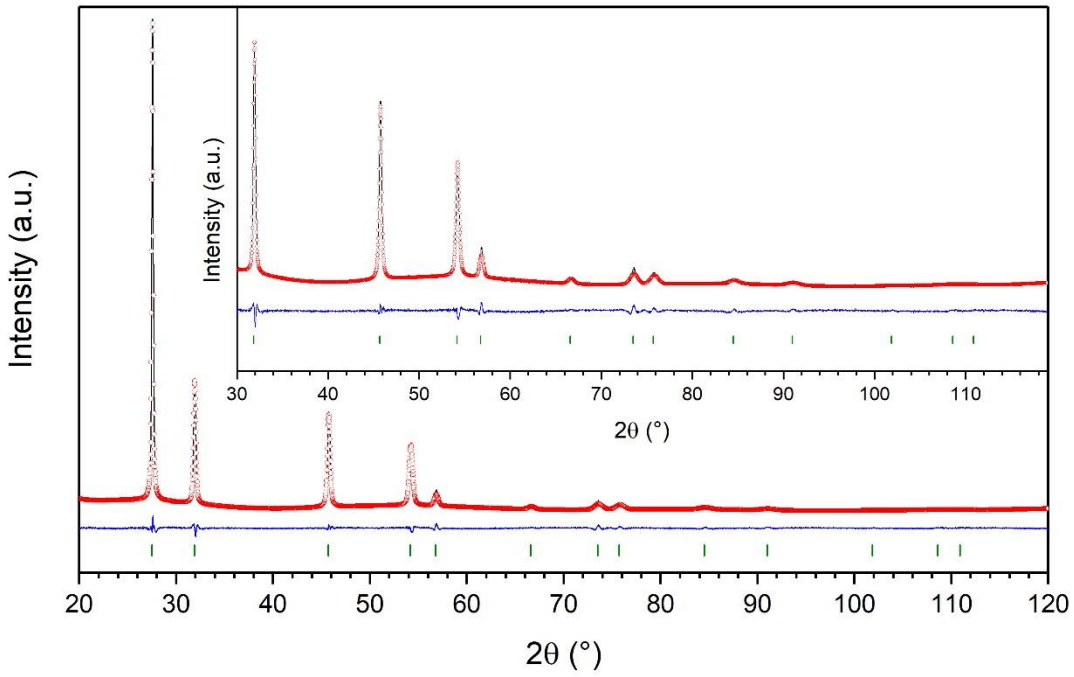

Figure 4. *Experimental (red circles), fitted (black solid line) and difference curve (blue solid line) of the XRD Rietveld diagram refinement of the* $Bi_{0.8}Nb_{0.8}Te_{2.4}O_8$ *anti-glass material using a site splitting model for the oxygen position (*192*l site). The inset corresponds to an enlargement of the same refined data. Reliability factors are* W_{Rp} *= 4.87%, GOF = 1.59,* R_p *= 3.70%.*

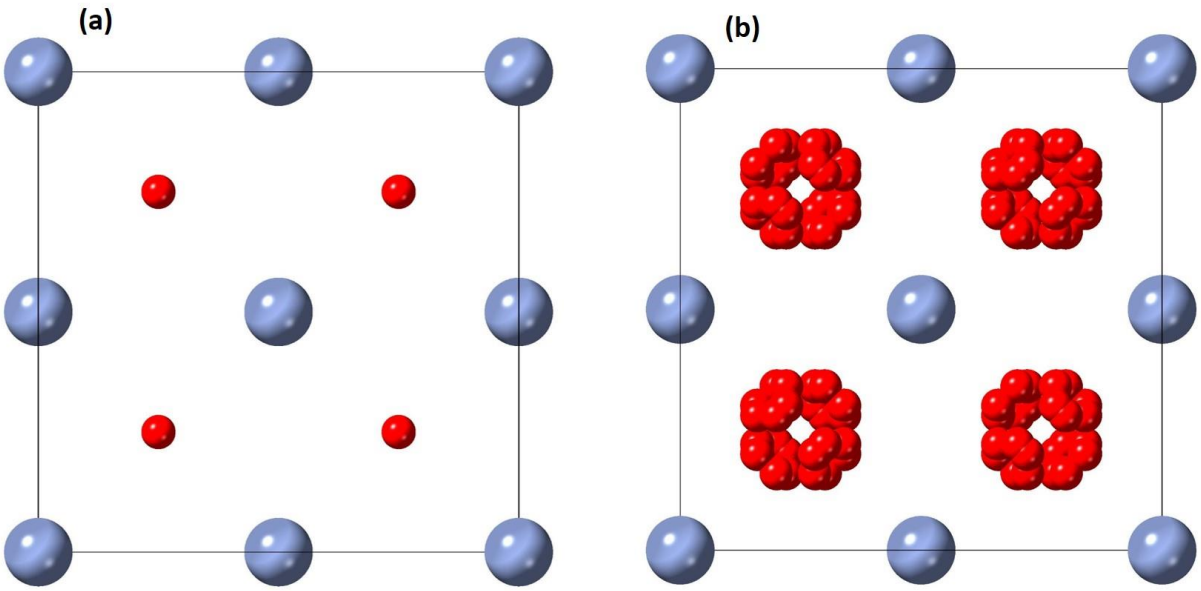

Figure 5. *Schematic [001] views of the $Bi_{0.8}Nb_{0.8}Te_{2.4}O_8$ anti-glass structure. The blue and red spheres denote mixed Bi/Nb/Te and O atoms, respectively. (a) The oxygen site was initially placed at the ¼ ¼ ¼ position (8c), as in the isostructural $Bi_2Te_4O_{11}$ model. (b) Given its very high Debye-Weller factor, the oxygen site was then freely refined to a lower symmetry 192l position (x,y,z) which illustrates the disorder on this crystallographic site, as expected for an anti-glass structure [16].*

The X-ray diffractogram of the $Bi_{0.8}Nb_{0.8}Te_{2.4}O_8$ ceramic phase shows extra reflections compared to that of the anti-glass phase, which indicates that structural ordering occurs when the heat treatment temperature increases, *i.e.* during the anti-glass to ceramic phase transition (Figure 1). In fact, the $Bi_{0.8}Nb_{0.8}Te_{2.4}O_8$ ceramic adopts the AB_3O_8-type structure, isostructural with the $TiTe_3O_8$ phase (Ia-3, a=11.2Å). It has 2 cationic sites (8a 0, 0, 0 for *A* and 24d x, 0, ¼ for *B*) and 2 oxygen sites (48e x,y,z and 16c x, x, x). The *A* site lies in an almost perfectly symmetric octahedral environment whereas the *B* site is located slightly off the plan formed by its 4 oxygen neighbours (the *B* site is usually occupied by Te^{4+} in AB_3O_8 structures, with the

Te^{4+} lone pair positioned opposite to the oxygen plan) [25]. AB_3O_8 can be described as a superstructure of the fluorite structure, with a unit cell made up of 2x2x2 fluorite cells and cations sit on a (distorted) face-centered cubic (FCC) lattice. The extra-reflections observed with the $Bi_{0.8}Nb_{0.8}Te_{2.4}O_8$ ceramic phase are thus superstructure reflections mainly coming from the ordering of the cations, initially randomly distributed on the FCC lattice.

Since the Bi^{3+}, Nb^{5+} and Te^{4+} cations can *a priori* occupy both *A* and *B* sites, it is not possible to determine the compositions of the cationic sites from powder diffraction data only. To overcome this limitation, ^{93}Nb NMR experiments were performed (see NMR section) and showed that Nb^{5+} is exclusively located on the octahedral *A* site (8a cationic site), *i.e.* that there is no Nb on the planar *B* site (24d cationic site). Therefore, in addition to fully occupied cationic sites restrictions, all Nb atoms were considered to occupy the octahedral 8a cationic site in subsequent Rietveld refinements.

In order to get more sensitivity on the cation distribution in the *A* and *B* sites and better accuracy on the oxygen positions, combined refinements of X-ray and neutron powder diffraction data were performed. Anisotropic line broadening had to be considered, as the superstructure reflections clearly appeared much broader than the intense ones (fundamental reflections) previously observed for the anti-glass material (Figure SI-2). The same broadening anisotropy was applied for both the X-ray and neutron powder diffraction refinements. The resulting Rietveld plots of both XRPD and NPD data are shown in Figures 6 and 7, respectively. The final refined structural parameters and interatomic distances of the $Bi_{0.8}Nb_{0.8}Te_{2.4}O_8$ ceramic are listed in Tables 4 and 5, while a view of the average structure is presented in Figure 8.

The *A* site appears to be occupied by 80% of Nb^{5+} (value fixed from nominal composition and NMR results), 13(1)% of Bi^{3+} and 7(1)% of Te^{4+}, whereas the *B* site is composed of 22(1)% of Bi^{3+} and 78(1)% of Te^{4+}. The $Bi_{0.8}Nb_{0.8}Te_{2.4}O_8$ structure formulae can therefore be written as $(Bi_{0.13}Te_{0.07}Nb_{0.8})(Bi_{0.67}Te_{2.33})O_8$ with respect to the AB_3O_8 structure. It appears that the Te^{4+}

cations much prefer to occupy the *B* cationic site with a position off the oxygens plan and only 3% of the Te atoms are found in the symmetric octahedral *A* cationic site. The remaining *B* sites are then occupied by 84% of the Bi^{3+} cations. This illustrates the preferential location of heavy cations with $5s^2$ and $6s^2$ lone pairs on the *B* sites of the structure [25].

The extra broadening observed for the superstructure reflections may certainly be attributed to the presence of antiphase domains in the ceramic phase. Indeed, we have seen above that in both the anti-glass and ceramic phases, cations sit on a FFC lattice. In the ceramic phase, they are ordered in such a way that Nb atoms occupy almost all the cube corners and the Te/Bi atoms occupy all the face-centre positions. However, as an equivalent FCC lattice can be formed starting from a cube corner or a face centre, it is likely that the cations ordering (e.g. Nb) starts at any one of these positions throughout the crystal, leading to the formation of anti-phase domains shifted by half the diagonal of a cube face. At the antiphase boundaries, the number of like and unlike nearest cations remains in that way almost unchanged, which consequently introduces only a small instability. A simple line broadening analysis of the superstructure reflections give an average integral breadth of 0.008 $Å^{-1}$ (reciprocal units) corresponding to an effective antiphase domain size of about 12 nm. This value is coherently well below the domain sizes observed with EBSD. Interestingly, this value does not change with increasing time thermal treatment time (i.e. from 5 min to 1h30 at 510°C).

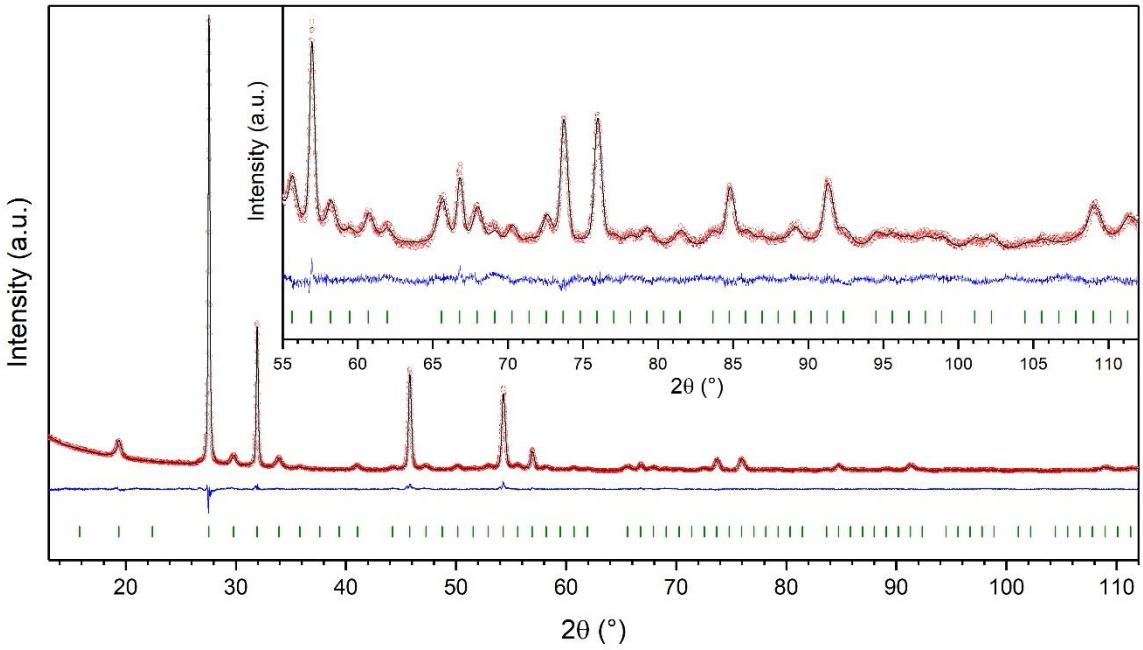

Figure 6. *Experimental (red circles), fitted (black solid line) and difference curve (blue solid line) of the XRD Rietveld diagram refinement of the* $Bi_{0.8}Nb_{0.8}Te_{2.4}O_8$ *ceramic material. The inset corresponds to an enlargement of the same refined data. Reliability factors are* R_B *= 4.38%,* R_F *= 2.37%,* χ^2 *= 2.47.*

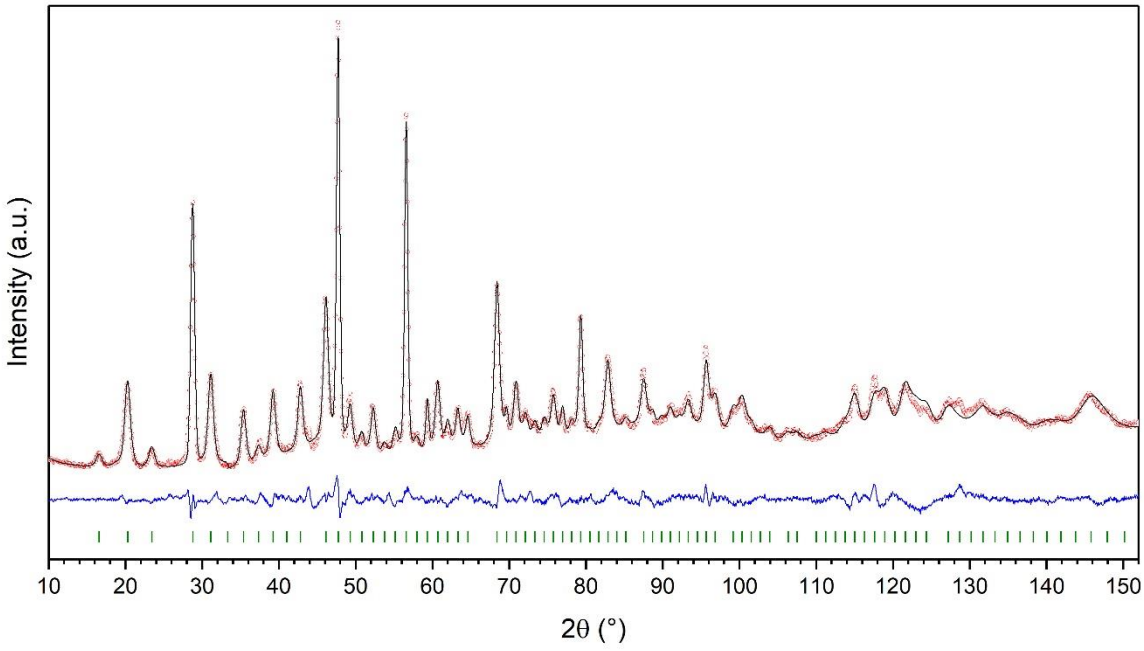

Figure 7. *Experimental (red circles), fitted (black solid line) and difference curve (blue solid line) of the NPD Rietveld diagram refinement of the* $Bi_{0.8}Nb_{0.8}Te_{2.4}O_8$ *ceramic material. Reliability factors are* $R_B = 4.45\%$, $R_F = 3.01\%$, $\chi^2 = 6.62$.

Table 4. *Atomic coordinates and occupancies determined for the* $Bi_{0.8}Nb_{0.8}Te_{2.4}O_8$ *ceramic phase from Rietveld refinement of both X-ray and neutron powder diffraction patterns collected at room temperature.*[a]

Atom	Site	x	y	Z	Occupancy	U_{iso} (Å^2)
Nb1	8a	0	0	0	0.800[b]	0.001(1)
Bi1	8a	0	0	0	0.133(5)	0.001(1)
Te1	8a	0	0	0	0.067(5)	0.001(1)
Te2	24d	0.2209(1)	0	0.25	0.778(5)	0.014(1)
Bi2	24d	0.2209(1)	0	0.25	0.222(5)	0.014(1)
O1	48e	0.4342(2)	0.1325(2)	0.3938(2)	1	0.025(1)
O2	16c	0.1723(2)	0.1723(2)	0.1723(2)	1	0.013(2)

[a] Space group Ia-3, a=11.1966(1) Å. [b] Fixed parameter.

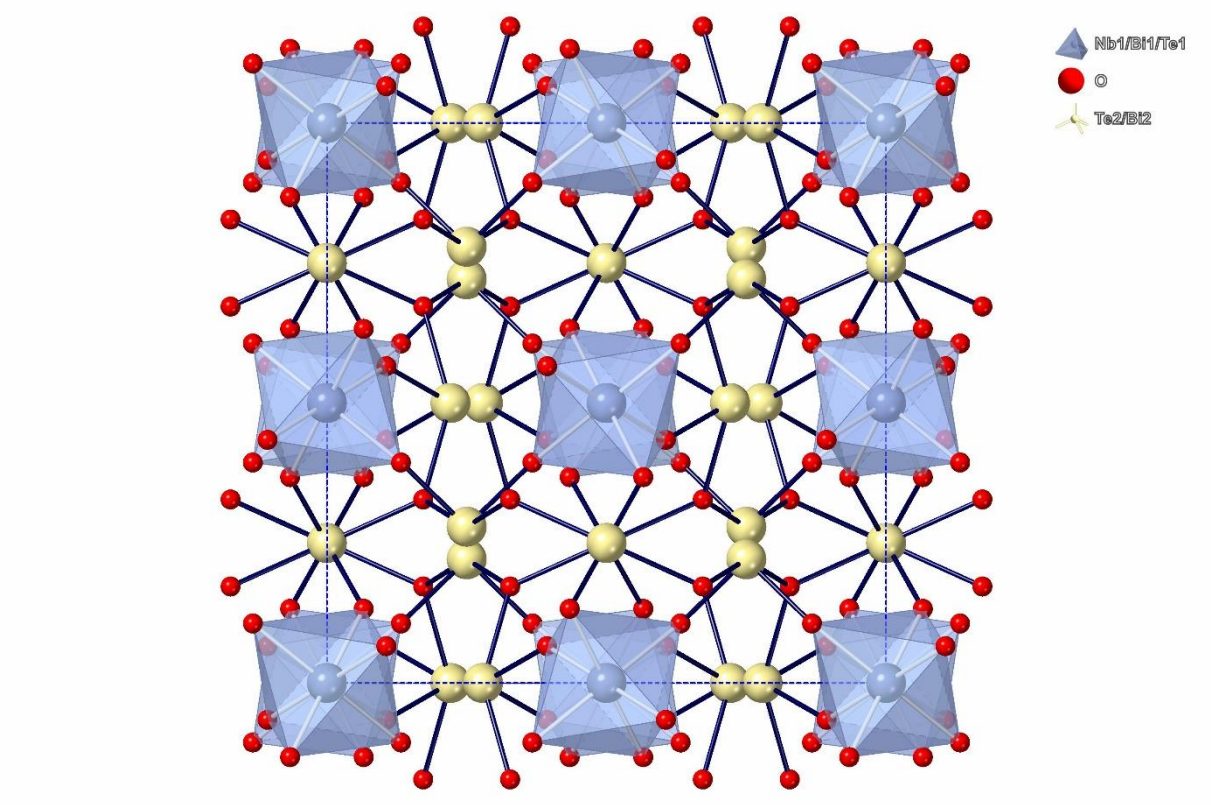

Figure 8. *Schematic [001] view of the $Bi_{0.8}Nb_{0.8}Te_{2.4}O_8$ ceramic structure. The blue, white and red spheres denote mixed Bi1/Nb1/Te1, Bi2/Te2 and O atoms, respectively.[16]*

Table 5. *Bond lengths for the $Bi_{0.8}Nb_{0.8}Te_{2.4}O_8$ ceramic phase from Rietveld refinement of both X-ray and neutron powder diffraction patterns collected at room temperature.*

Bond	**Length (Å)**
Nb1/Bi1/Te1 – O1 (x6)	2.038(3)
Bi2/Te2 – O1 (x2)	1.982(3)
Bi2/Te2 – O2 (x2)	2.185(2)

^{93}Nb and ^{125}Te solid-state NMR experiments were performed to further investigate the local environments of the cations and their distributions in the $Bi_{0.8}Nb_{0.8}Te_{2.4}O_8$ glass, anti-glass and ceramic materials.

As shown in Figure 9, the ^{93}Nb central-transition (CT) MAS spectra of the three samples recorded at high magnetic field (20.0 T) exhibit a single intense resonance and several associated spinning sidebands of weaker intensities. The position of the centerband is located at *ca.* -1050 ppm, characteristic of six-fold coordinated environments in niobium oxides [28]. For the three samples, two-dimensional MQMAS experiments reveal that the line broadening results from distributions of the ^{93}Nb quadrupolar coupling and isotropic chemical shift (SI-3). For the glass, a large isotropic chemical shift (CS) distribution (ΔCS≈150 ppm) associated to an average quadrupolar coupling constant of ~ 43 MHz is observed, reflecting the distribution of NbO_6 environments (variations of bond lengths, bond angles, next-nearest neighbours) in the disordered network. As a noticeable feature, the distribution of ^{93}Nb NMR parameters for the anti-glass material remain similar to those of the glass, while diffraction data indicate average long-range ordering. This clearly illustrates the peculiar nature of the anti-glass structure. In contrast, the ^{93}Nb isotropic CS distribution measured for the ceramic material is two times smaller (ΔCS≈70 ppm) reflecting significant ordering of the network, even if some distribution of the Nb local environment remains due to the Te/Bi substitutions on the *B* shared site of the AB_3O_8 structure (Nb only in the *A* site).

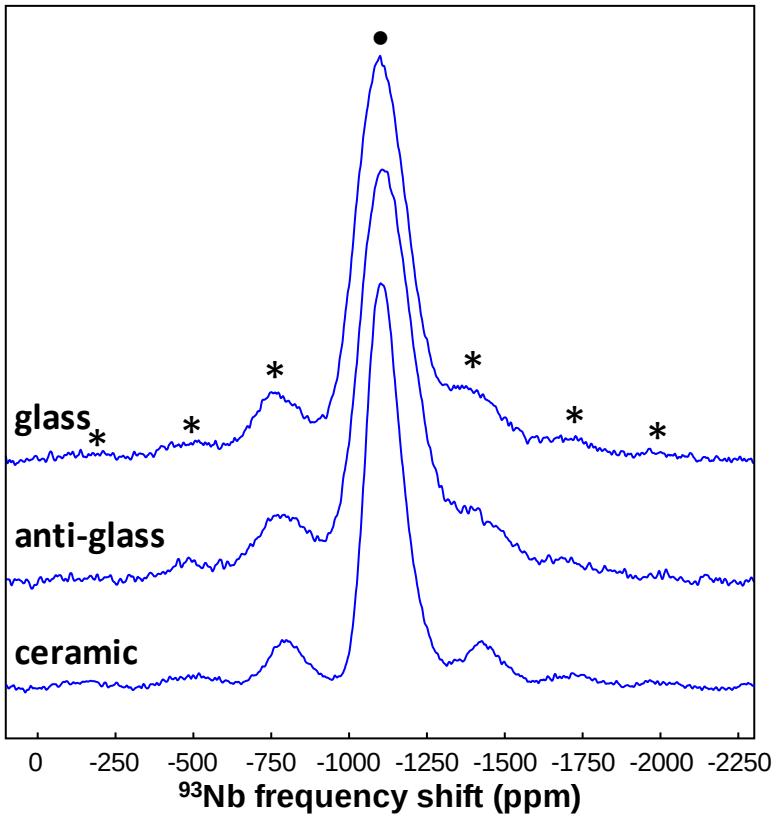

Figure 9. *^{93}Nb MAS NMR spectra (in blue) recorded at 20 T with a MAS frequency of 65 kHz for the glass (top), anti-glass (middle) and ceramic (bottom) BNT samples. The full circle and the stars denote the isotropic line and the spinning sidebands of the central transition, respectively (see SI-4 for the reconstructed spectra).*

The ^{125}Te static spectrum of the glass (Figure 10) exhibits a broad asymmetric lineshape indicating a strong chemical shift anisotropy typical of both TeO_4 and TeO_3 environments [29, 30]. The ^{125}Te MAS spectrum is similar to the static one due to a large isotropic chemical shift distribution (larger than the spinning frequency) leading to a full overlap of spinning sidebands. As in the case of niobium, the ^{125}Te NMR spectra obtained for the anti-glass phase are almost identical to those of the glass, suggesting that the whole distribution of Te environment remains preserved after the average long-range cationic ordering occurring at 460 °C. In contrast, a modification of the static lineshape and a narrowing of the spinning sidebands in the MAS

spectrum are clearly observed for the ceramic, indicating a significantly smaller distribution of Te environments.

To further describe the Te local structures, two-dimensional PASS NMR experiments allowing separate measurements of the ^{125}Te isotropic and anisotropic chemical shift distributions were performed (see SI-5). The ^{125}Te isotropic spectra obtained for the glass and the anti-glass are nearly identical (Figure 10), showing a Gaussian lineshape centered at $\delta_{iso}\approx$1600 ppm with a FWHM of ca. 300 ppm. In both cases, the ^{125}Te isotropic CS distribution covers the ranges reported for TeO_4 (1450-1650 ppm), TeO_{3+1} (1600-1680 ppm) and TeO_3 (1650-1850 ppm) units [30]. This assignment is consistent with the chemical shift anisotropy (CSA) values (obtained from spinning sideband intensities in 2D PASS spectra) which are also almost identical for the glass and the anti-glass (Figure 11). The distribution of Te coordinations (and associated distribution of Te-O bond lengths) observed in the glassy phase is thus kept in the anti-glass structure, testifying for the presence of a strongly disorder anionic sub-network. Coexistence of long-range ordered cationic and disordered anionic sub-networks in the anti-glass phase is likely related to the presence of heavy and highly polarizable cations (Te^{4+}, Bi^{3+}) with lone-pair electrons and their local bonding adaptabilities. For the ceramic, the ^{125}Te isotropic CS distribution decreases by a factor 2 (FWHM~140 ppm), evidencing chemical ordering around tellurium, and a shift toward smaller CS values (~1460 ppm) is observed in agreement with the location of Te in the *B* site forming TeO_4 units. The remaining isotropic CS distribution reflects random substitution effects in adjacent octahedral *A* and planar *B* cationic sites, consistent with the proposed average model (Te/Bi in site *B,* mainly Nb/Bi in site *A*). It should be noted that the ^{125}Te spectra do not show any signal corresponding to TeO_6 units, while 3% of the Te atoms are expected to occupy the octahedral *A* site in the average model resulting from Rietveld refinements. Instead, a weak intensity line is observed with higher isotropic CS and CSA values typical of TeO_{3+1}/TeO_3 coordinations (Figure 11). Indeed, the occupancy of *A* sites by lone-pair

cations like Te or Bi is expected to lead to strong local distortions and modifications of the *A* site coordination polyhedron, due to the steric hindrance of the lone pair and its interactions between adjacent lone-pair cations located in *B* sites. This weak intensity peak is thus assigned to Te in distorted *A* sites and also to Te in *B* sites with adjacent distorted *A* sites (i.e. occupied by Bi or Te).

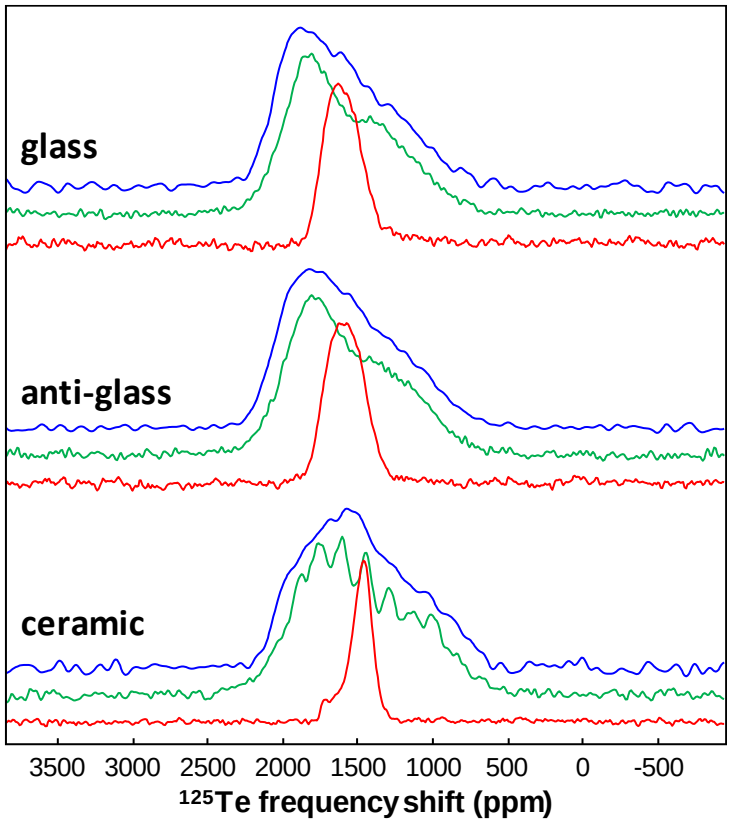

Figure 10. *^{125}Te NMR spectra recorded at 7 T for the glass (top), anti-glass (middle) and ceramic (bottom) BNT samples. In blue: static spectrum; in green: MAS spectrum (MAS frequency of 14285 Hz); in red: isotropic spectrum obtained from the PASS experiment (see SI-5 for the 2D spectra).*

To summarize, ^{93}Nb and ^{125}Te solid state NMR spectra show that the glass to anti-glass phase transition, which leads to an average long-range topological ordering of the cations as evidenced

by diffraction, does not modify the distributions of niobium and tellurium local environments (first and second coordination shells) observed for the glass. Such feature involves strong disorder in the anionic sub-network and is likely associated to the presence of heavy cations with high polarizabilities. During the ceramisation step occuring at 510°C, ordering of the oxygen sub-network takes place. The remaining ^{93}Nb and ^{125}Te CS distributions reflect mostly cationic substitution effects in the second coordination shell of *A* and *B* sites, consistent with the average structural model. Occupancy of the *A* site by Te or Bi lone-pair cations leads to strong local distortion of its coordination polyhedra.

.

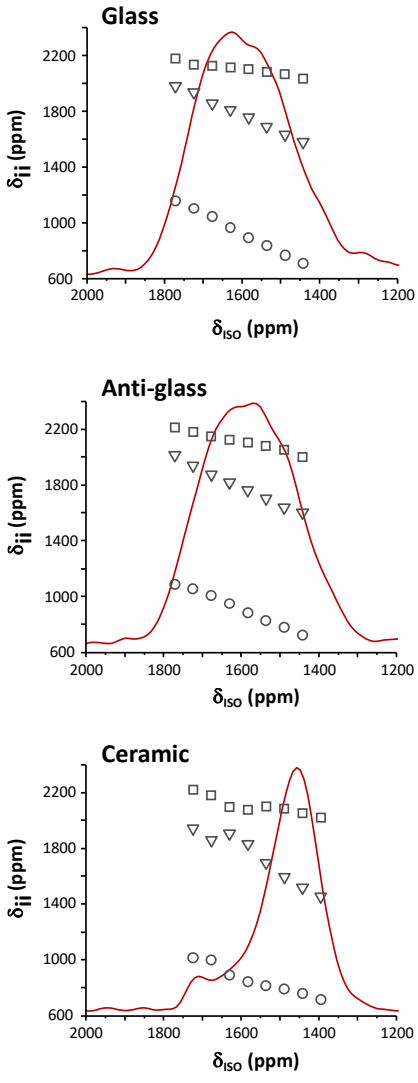

Figure 11. *Principal values of the ^{125}Te CSA tensor (δ_{ii}) as a function of isotropic CS (δ_{iso}) values taken across the ^{125}Te isotropic CS distribution (red line) of the glass (top), anti-glass (middle) and ceramic (bottom) BNT materials. Squares, triangles and circles correspond to δ_{11}, δ_{22} and δ_{33}, respectively, with $|\delta_{33}-\delta_{iso}|>|\delta_{11}-\delta_{iso}|>|\delta_{22}-\delta_{iso}|$ and $\delta_{iso}=(\delta_{11}+\delta_{22}+\delta_{33})/3$.*

3.2 Microstructure study

TEM images of the anti-glass (460°C, 15 min) and ceramics (510°C, 5 min and 1h30) recorded on FIB-prepared samples are presented in Figures 12, 13 and 14.

The anti-glass microstructure exhibits some large domains of about ~ 500-700 nm (Figure 12a). The dark and light grey regions regarding the Bright Field TEM image (Figure 12a) is only related to diffraction contrast and not crystalline (dark grey)/amorphous (light grey) contrast. Diffraction contrast in different grains happens due to different orientations and when grains are oriented close to strong Bragg- reflections than others, they appear darker as a consequence of diffraction contrast. This observation is confirmed by SAED patterns of both dark and light grey areas that show polycrystalline ring patterns (Figure 12d, e). One can observe bright spots and diffuse rings showing the partial ordering of the anti-glass phase. The size of these domains is consistent with the EBSD images recorded on the same sample (Figure 2a). Each domain is moreover constituted of smaller grains (~ 50 nm) as depicted in Figure 12b, giving rise to a complex multi-scale microstructure. High resolution transmission electron microscope (HRTEM) image (Figure 12c) shows the existence of an intermediate nanostructure between amorphous and crystalline areas, characteristic of an anti-glass, as depicted by FFT patterns (inset of Figure 12c). For example, some atomic planes (FFT orientations (311) and (111) of the cubic phase, space group Fm-3m, a=5.6Å) superimpose a more random structure while local ordering seems to take place in Figure 12c. These observations correspond to the anti-glass

formation. Interestingly, while first observations suggested a full and congruent crystallization from the parent glass, the STEM-HAADF imaging and STEM-EDS maps reveal some bismuth depletion between ~50 nm grains (Figure 12f).

The microstructures of the ceramic samples heat-treated at 510°C for 5 minutes and 1h30 appear similar (Figures 13 and 14). Large domains constituted of smaller grains can still be observed. The HRTEM images exhibit atomic planes and narrow grain boundaries (~ 2 nm) (Figure 13b). The previous bismuth depletion observed in the anti-glass phase is less pronounced here, indicating higher chemical homogeneity in ceramic samples (510°C, 5 min and 1h30). The FFT indexations are consistent with the cubic phase structure proposed in the previous section (space group Ia-3, a=11.2Å). Some porosities (~ 20 nm) can be detected, especially in the ceramic heat-treated at 510°C for 1h30 (Figure 14c, d). This porosity may arise from the differences in density values of both glass and ceramic samples (6.00(2), 6.20(2) and 6.27(2) g.cm^{-3} for the glass, anti-glass and ceramic respectively). Nevertheless, given its nanometer scale this porosity does not affect much the visible/NIR transmission and lasing properties [17, 18].

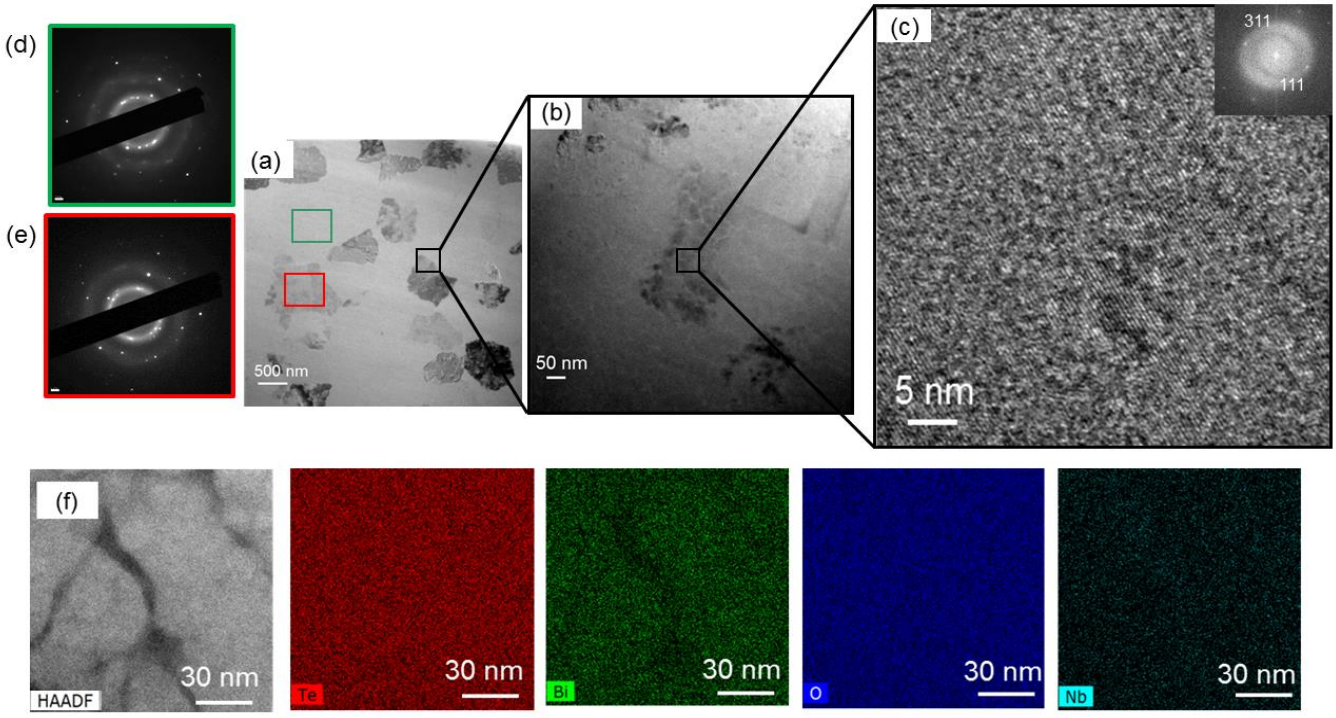

Figure 12. *BNT anti-glass 460°C 15 min (a), (b) Bright Field TEM micrographs of the multiscale microstructure, (c), HRTEM image and corresponding FFT pattern showing the complex mixing between amorphous and crystalline areas, (d), (e) Selected Area Electron Diffraction patterns of the light and dark grey areas respectively (f) STEM-HAADF image (Z-contrast) and STEM-EDX elemental maps highlighting a Bi depletion grains.*

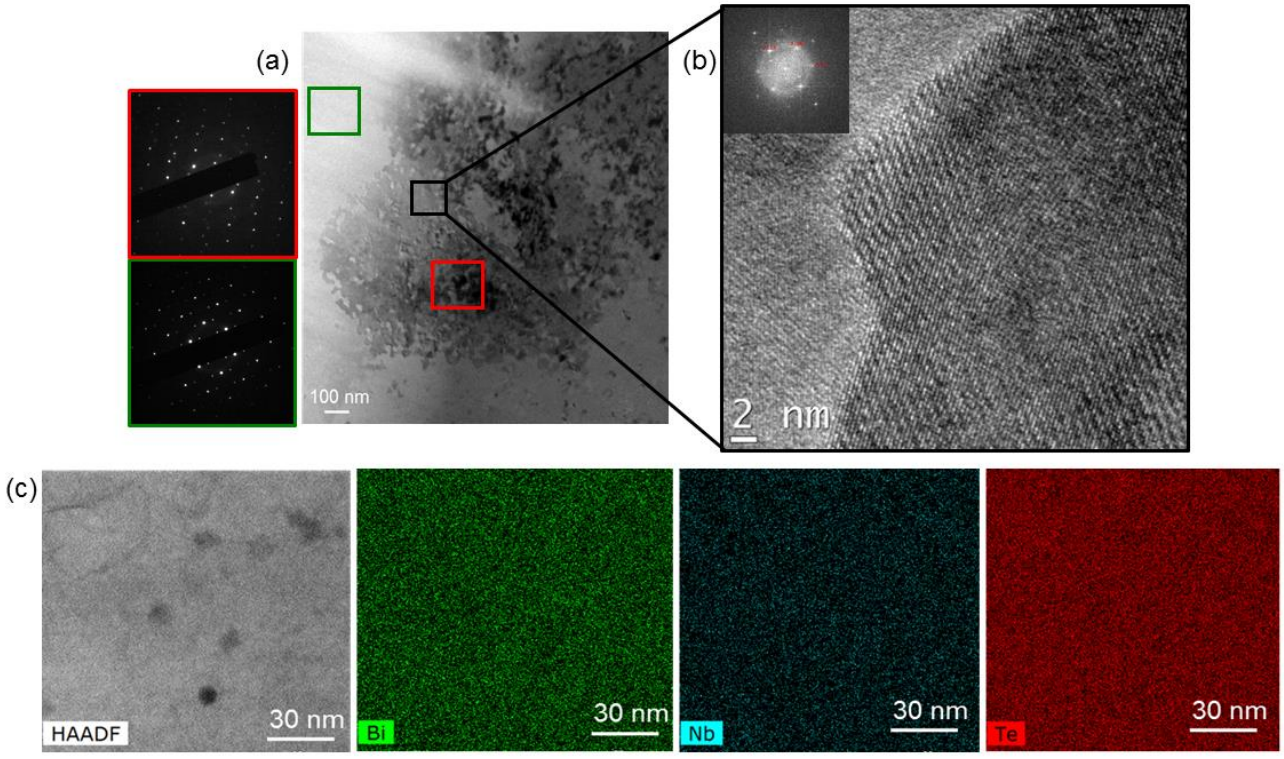

Figure 13. *BNT ceramic 510°C 5 min (a) Bright Field TEM micrograph showing large domains constituted of smaller grains and corresponding Selected Area Electron Diffraction patterns, (b) HRTEM image exhibits crystalline plans and narrow grain boundary, (c) STEM-HAADF image (Z-contrast) and STEM-EDS elemental maps showing a better chemical homogeneity compared to the anti-glass (Figure 12).*

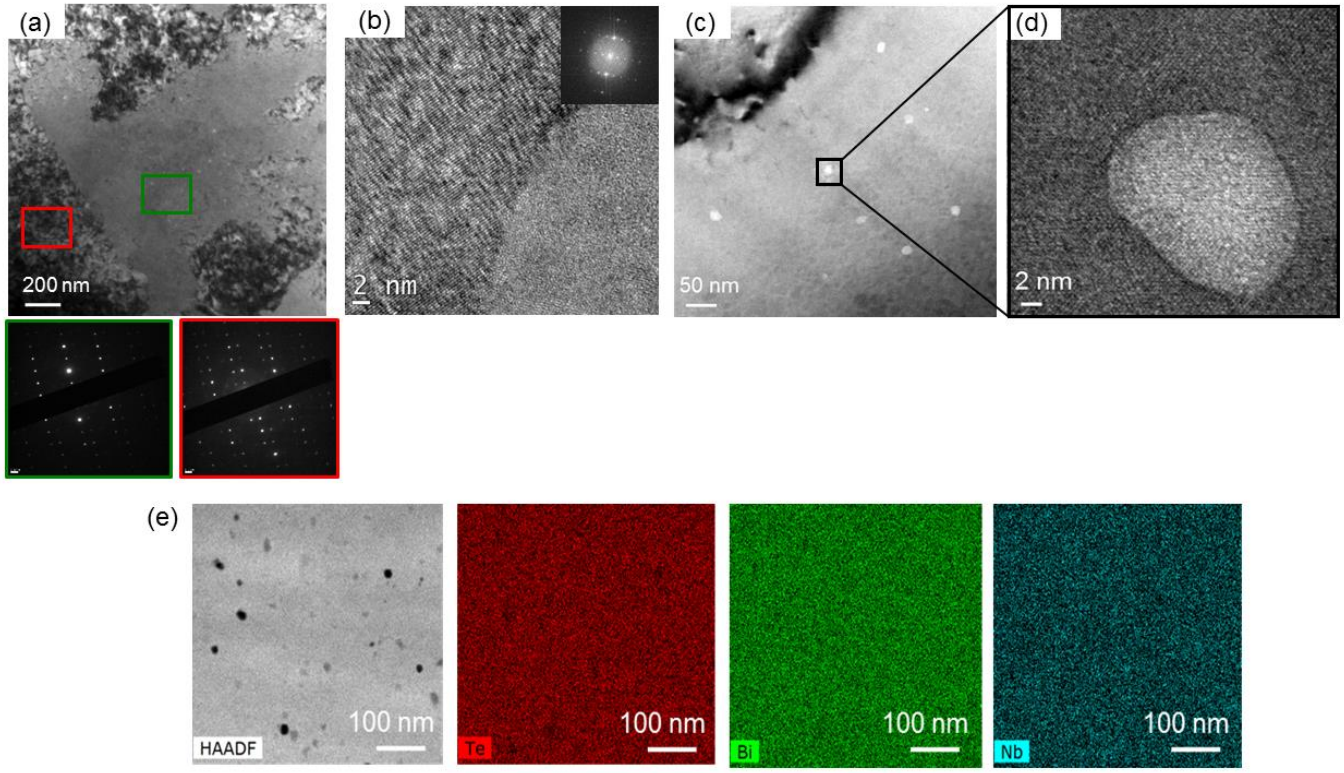

Figure 14. *BNT ceramic 510°C 1h30 (a) (b) Bright Field TEM and HRTEM micrographs showing large domains constituted of smaller grains and corresponding Selected Area Electron diffraction patterns, (c) (d), Bright Field TEM and HRTEM micrographs of porosity, (e) STEM-HAADF image (Z-contrast) and STEM-EDS elemental maps showing a better chemical homogeneity compared to the anti-glass (Figure 12).*

3.3 Optical properties of BNT samples

As shown in Figure 1, the ceramic heat-treated at 510°C for 1h30 retains an outstanding transparency while the anti-glass material shows important scattering effects. However, both of these phases exhibit cubic structures. To explain such different optical behaviors, two main reasons can be invoked. First, in the case of the anti-glass material, the presence of residual

glass located at grain boundaries cannot be excluded as shown by EBSD experiments (Figure 2), SAED patterns (Figure 12d, e) and EDS maps (Figure 12f). As glass and anti-glass samples do show different refractive indices (see Table SI-2), this should induce some birefringence, hence provoking scattering effects. Then, one can observe the microstructure and especially the chemical inhomogeneity at the nanometric scale, more pronounced in the case of the anti-glass phase (Cf. some Bi depletion is observed at the grain boundaries in the corresponding STEM-EDS map). Such depletion modifies locally the refractive index and will be again responsible for scattering phenomenon. [31]

Furthermore, some additional comment can be made on the evolution of the refractive indices, which vary from 2.166 for the glassy sample up to 2.230 in the case of the transparent ceramic (with a value of 2.221 reported for the anti-glass – see Table SI-2). In fact, such an increase is directly related to the concomitant density increase (the latter varying as follow: 6.00, 6.20 and 6.27 $g.cm^{-3}$ for the glass, anti-glass and ceramic, respectively).

Finally, from the optical transmission data (Figure 1c), it is also possible to derive the optical band gap value (E_g) (see Table SI-2). One can easily evidence the progressive reduction the E_g value from 3.16 down to 2.91 eV, while transforming the glass sample into the transparent ceramic, via the intermediate anti-glass phase (3.03 eV). Such decrease of E_g reflects of course the modification of the electronic structure occurring with the two consecutive transformations, and is as well in agreement with the different visual aspects of the samples. Indeed, one can easily notice the change in the color of the samples; the glass sample being clearer than the two other ones, which show a brownish-yellowish coloration.

4. Conclusion

The heat-treatment of the $Bi_{0.8}Nb_{0.8}Te_{2.4}O_8$ tellurite glass parent glass at 460°C and 510°C leads to a disordered anti-glass and more ordered ceramic phases, respectively, the latter material

showing an outstanding transparency. The combination of X-ray and neutron powder diffraction, solid-state NMR and Raman measurements reveals that the glass to anti-glass transition gives rise to an average long-range topological ordering of the cations without modifying the distributions of niobium and tellurium local environments observed in the glass. The ceramic obtained at higher temperature exhibits an AB_3O_8 structure type. Nb and Te atoms occupy preferentially the octahedral *A* sites and the deformed square planar *B* sites, respectively, and the remaining vacant A and B sites are occupied by Bi atoms. The location of lone-pair cations (Bi, Te) in *A* sites leads to strong local distortion of the coordination polyhedron due to steric hindrance and interactions between lone pairs. Both anti-glass and ceramic materials exhibit a complex multi-scale microstructure made of micrometric grains, each of them being constituted of nano-domains as observed in TEM experiments. While the ceramic material is chemically homogeneous at the micrometric scale, the anti-glass shows areas with Bi depletion at the origin of scattering phenomena. Such an anti-glass phase can thus be seen as an intermediate step to understand the full and congruent crystallization from the parent glass.

Acknowledgements

Financial support from the ANR “Investissements d’avenir” program TEMPOS (ANR-10-EQPX-50) and the TGIR-RMN-THC Fr3050 CNRS for conducting the research is gratefully acknowledged

References

[1] R. A. H. El-Mallawany, Tellurite Glasses Handbook: Physical Properties and Data 2002 CRC Press.

[2] J. S. Wang, D. P. Machewirth, F. Wu, E. Snitzer, and E. M. Vogel, "Neodymium-doped tellurite single-mode fiber laser", Optics Letters, 19 (1994) 1448-1449.

[3] Y. Tsang, B. Richards, D. Binks, J. Lousteau, A. Jha, "Tm^{3+}/Ho^{3+} codoped tellurite fiber laser", Optics Letters, 33 (2008) 1282-1284.

[4] C. Dunn, F. Kong, G. Gu, T. W. Hawkins, M. Jonas, J. Parsons, A. Runnion, M. T. Kalichevsky-Dong, R. Salem, D. Liu, D. Gardner, P. Fendel, R. Synowicki, E. Cheung, J. T. Gomes, L. Lavoute, D. Gaponov, S. Février, L. Dong, "Solid tellurite optical fiber based on stack-and-draw method for mid-infrared supercontinuum generation", Fibers, 5 (2017) 37-48.

[5] D. Rhonehouse, J. Zong, D. Nguyen, R. Thapa, K. Wiersma, C. Smith, A. Chavez-Pirson, "Low loss, wide transparency, robust tellurite glass fibers for mid-IR (2–5 μm) applications" Proc. SPIE (2013) 8898, 88980D.

[6] A. Bertrand, J. Carreaud, G. Delaizir, M. Shimoda, J. R. Duclère, M. Colas, M. Belleil, J. Cornette, T. Hayakawa, C. Genevois, E. Veron, M. Allix, S. Chenu, F. Brisset, P. Thomas "New transparent glass-ceramics based on the crystallization of "anti-glass" spherulites in the Bi_2O_3-Nb_2O_5-TeO_2 system", Crystal Growth and Design, 15 (2015) 5086-5096.

[7] M. C. Wilding, G. Delaizir, C. J. Benmore, Y. Gueguen, M. Dolhen, J.-R. Duclere, S. Chenu, S. Sukenaga, P. F. McMillan, "Structural studies of Bi_2O_3-Nb_2O_5-TeO_2 glasses", 451 (2016) 68-76.

[8] N. Gupta, A. Khanna, « Glass and anti-glass phase co-existence and structural transitions in bismuth tellurite and bismuth niobium tellurite systems", J. Non-Cryst Sol. 481 (2018) 594-603.

[9] S. Aasland, P. F. McMillan, "Density-driven liquid-liquid phase separation in the system Al_2O_3-Y_2O_3", Nature 369 (1994) 633-636.

[10] N. K. Nasikas, S. Sen, G. N. Papatheodorou, “Structural nature of polyamorphism in Y_2O_3-Al_2O_3 glasses”, Chemistry of materials 23 (2011) 2860–2868.

[11] P. F McMillan, M. Wilson, M. C. Wilding, D. Daisenberger, M. Mezouar, G. Neville Greaves, “Polyamorphism and liquid–liquid phase transitions: challenges for experiment and theory”, Journal of Physics: Condensed Matter 19 (2007) 415101.

[12] G. N. Greaves, M. C. Wilding, S. Fearn, D. Langstaff, F. Kargl, S. Cox, Q. Vu Van, O. Majérus, C. J. Benmore, R. Weber, C. M. Martin, L. Hennet, “Detection of First-Order Liquid/Liquid Phase Transitions in Yttrium Oxide–Aluminum Oxide Melts”, 322 (2008) 566-570.

[13] H. G Burckhardt, M. Trömel, “Strontium-undecaoxotellurat, $SrTe_5O_{11}$, eine CaF_2-Defektstruktur und ihre Beziehung zur Struktur einfacher Gläser”, Acta Cryst. C, C39 (1983) 1322-1323.

[14] M. Trömel, W. Hützler, E. Münch, “Anti-glass phases and other lanthanide tellurates with fluorite-related structures”, Journal of the Less Common Metals, 110 (1985) 421-424.

[15] M. Trömel, E. Münch, G. Blasse, G.J. Dirksen, “Formation and luminescence of lower symmetrical tellurite anti-glass phases”, Journal of Solid State Chemistry, 76 (1988) 345-354.

[16] O. Masson, P. Thomas, O. Durand, T. Hansen, J. C. Champarnaud, D. Mercurio, “On the structure of the disordered $Bi_2Te_4O_{11}$ phase”, Journal of Solid State Chemistry, 177 (2004) 2158-2176.

[17] A. Bertrand, J. Carreaud, S. Chenu, M. Allix, E. Véron, J. ‐ R. Duclère, Y. Launay, T. Hayakawa, C. Genevois, F. Brisset, F. Célarié, P. Thomas, G. Delaizir, ″Scalable and Formable Tellurite ‐ Based Transparent Ceramics for Near Infrared Applications″, Advanced Optical Materials, 4 (2016) 1482-1486.

[18] M. Dolhen, M. Tanaka, V. Couderc, S. Chenu, G. Delaizir, T. Hayakawa, J. Cornette, F. Brisset, M. Colas, P. Thomas, J.-R. Duclère, "Nd^{3+}-doped transparent tellurite ceramics bulk lasers", Scientific Reports, 8 (2018) 4640.

[19] S. Wen, Y. Wang, B. Lan, W. Zhang, Z. Shi, S. Lv, Y. Zhao, J. Qiu, S. Zhou, "Pressureless Crystallization of Glass for Transparent Nanoceramics", Advanced Science, (2019) 1901096.

[20] V. Petrícek, M. Dušek, L. Palatinus, L. Crystallographic computing system JANA2006: general features. Z. Krist. 229 (2014) 345–352.

[21] J. Rodríguez-Carvajal, Recent Developments of the Program FULLPROF, in Commission on Powder Diffraction (IUCr).Newsletter 26 (2001) 12-19.

[22] D. Massiot, B. Touzo, D. Trumeau, J. P. Coutures, J. Virlet, P. Florian, P. J. Grandinetti, Solid State Nucl. Magn. Reson. 6 (1996) 73-83.

[23] F. Fayon, C. Bessada, A. Douy, D. Massiot, J. Magn. Reson. 137 (1999) 116-121.

[24] D. Massiot, F. Fayon, M. Capron, I. J. King, S. Le Calve, B. Alonso, J. O. Durand, B. Bujoli, Z. Gan, G. Hoatson, Magn. Reson. Chem. 40 (2002) 70-76.

[25] G. Meunier, J. Galy, P. Hagenmuller, "Sur une nouvelle série de composés de formule $A_{0.5}B_{0.5}Te_3O_8$ de type structural $TiTe_3O_8$ (A=Sc, Cr, Fe, Ga, Rh, In, Bi et B=Nb, Ta)", C. R. Acad. Sc., 270 (1970) 1987-1990.

[26] T.Vasileiadis, S.N. Yannopoulos, J.Appl.Phys. 116 (2014) 103510.

[27] M. R. Zaki, D. Hamani, M. Dutreilh-Colas, J-. R. Duclère, J. de Clermont-Gallerande, T. Hayakawa, O. Masson, P. Thomas, J. of Non-Cryst. Solids 512 (2019) 161-173.

[28] O.B. Lapina, D.F. Khabibulin, A.A. Shubin, V.V. Terskikh, "Practical aspects of 51V and 93Nb solid-state NMR spectroscopy and applications to oxide materials", Progress in Nuclear Magnetic Resonance Spectroscopy 53 (2008) 128–191.

[29] M. N. Garaga, U. Werner-Zwanziger, J. W. Zwanziger, "125Te NMR Probes of Tellurium Oxide Crystals: Shielding-Structure Correlations", Inorganic Chemistry, 57 (2018) 892-898.

[30] S. Sakida, S. Hayakawa, T. Yoko, J. Non-Cryst. Solids 243 (1999) 1-12.

[31] R. Apetz and M. P. B. Van Bruggen, "Transparent alumina: A light-scattering model," Journal of the American Ceramic Society, 86 (2003) 480-86.